Local Disorder-Induced Elevation of Intrinsic Anomalous Hall Conductance in an Electron-Doped Magnetic Weyl Semimetal

Jianlei Shen,[1,2,*] Qiushi Yao,[3,*] Qingqi Zeng,[1,2] Hongyi Sun,[3] Xuekui Xi,[1] Guangheng Wu,[1] Wenhong Wang,[1,4] Baogen Shen,[1,5] Qihang Liu,[3,6,7,†] and Enke Liu[1,4,‡]

[1]*State Key Laboratory for Magnetism, Institute of Physics, Chinese Academy of Sciences, Beijing 100190, China*
[2]*School of Physical Sciences, University of Chinese Academy of Sciences, Beijing 100049, China*
[3]*Shenzhen Institute for Quantum Science and Technology and Department of Physics, Southern University of Science and Technology, Shenzhen 518055, China*
[4]*Songshan Lake Materials Laboratory, Dongguan, Guangdong 523808, China*
[5]*Institute of Rare Earths, Chinese Academy of Sciences, Jiangxi 341000, China*
[6]*Guangdong Provincial Key Laboratory for Computational Science and Material Design, Southern University of Science and Technology, Shenzhen 518055, China*
[7]*Shenzhen Key Laboratory of for Advanced Quantum Functional Materials and Devices, Southern University of Science and Technology, Shenzhen 518055, China*

(Received 16 February 2020; revised 14 May 2020; accepted 10 July 2020; published 20 August 2020)

Topological materials are expected to show distinct transport signatures owing to their unique band-inversion characteristic and band-crossing points. However, the intentional modulation of such topological responses through experimentally feasible means has yet to be explored in depth. Here, an unusual elevation of the anomalous Hall effect (AHE) is obtained in electron (Ni)-doped magnetic Weyl semimetals $Co_{3-x}Ni_xSn_2S_2$, showing peak values in the anomalous Hall-conductivity, Hall-angle, and Hall-factor at a relatively low doping level of $x = 0.11$. The separation of intrinsic and extrinsic contributions using the TYJ scaling model indicates that such a significant enhancement is dominated by the intrinsic mechanism of the electronic Berry curvature. Theoretical calculations reveal that compared with the Fermi-level shifting from electron filling, a usually overlooked effect of doping, that is, local disorder, imposes a striking effect on broadening of the bands and narrowing of the inverted gap, thus resulting in an elevation of the integrated Berry curvature. Our results not only realize an enhancement of the AHE in a magnetic Weyl semimetal, but also provide a practical design principle for modulating the bands and transport properties in topological materials by exploiting the local disorder effect from doping.

DOI: 10.1103/PhysRevLett.125.086602

As a pseudomagnetic field in the momentum space, the Berry curvature describes the geometric phase of the wave function [1,2]. In magnetic materials with broken time-reversal symmetry, the integration of the Berry curvature of all occupied states through the entire Brillouin zone (BZ) adds a transverse velocity term into the equation of motion, giving rise to an intrinsic contribution to the anomalous Hall conductivity (AHC) [2,3]. In topological materials, the nontrivial Berry curvature is expected to significantly contribute to the anomalous Hall effect (AHE) and the relevant physical properties. A magnetic Weyl semimetal $Co_3Sn_2S_2$ was recently discovered experimentally [4–8], with a significant AHC of ~1130 Ω^{-1} cm^{-1} and an anomalous Hall angle (AHA) of ~20%. The measured AHC is highly consistent with the theoretical calculations from the Berry curvature, indicating that the AHC is dominated by intrinsic contribution originating from the clean nontrivial Weyl bands around the Fermi level (E_F) [4].

How can the transverse transport effects, like the AHC in magnetic topological materials, be further enhanced, particularly in $Co_3Sn_2S_2$ that already has a giant effect? According to the Kubo formula [9], the intrinsic AHC is closely related to two factors. One is the electron occupation determined by the position of E_F, and the other is the topological band characteristic around E_F, such as the size of the inverted band gap. We consider the possibility of doping, which has been well established as a way to control the material properties. In $Co_3Sn_2S_2$, it has been predicted that the position of E_F is already optimal for the integrated Berry curvature [4], implying that within the rigid band framework [10], doping is not expected to further elevate the intrinsic AHC. However, in addition to the voltage gating effect [11,12], chemical doping induces modulation of the electronic structure, which is often overlooked. For example, a disordered distribution of the dopants will change the local potential environment and destroy the translational symmetry [13,14], inevitably modifying the band structure and affecting Berry curvature. Meanwhile, the introduction of alien atoms may cause the impurity scattering, which usually generates an

extrinsic contribution [15]. Therefore, the physical mechanism of how doping affects the AHC in topological materials is intricate and therefore requires a comprehensive exploration.

In this Letter, based on experimental measurements, transport scaling, and chemical-doping theory encoded in first-principles calculations, we found that in $Co_{3-x}Ni_xSn_2S_2$ with low doping concentrations ($x \leq 0.1$), a disorder-induced band gap narrowing dominates the modulation of the Berry curvature, leading to a sizable enhancement of AHC of up to 60% compared with the undoped sample. Scaling model shows that such an enhancement of AHC is mainly from intrinsic rather than extrinsic contributions. Our work demonstrates that a local disorder can be used to engineer the desired physical properties through an intrinsic Berry curvature design.

To probe the evolution of AHC with the Ni substitution of Co, a series of single crystals of $Co_{3-x}Ni_xSn_2S_2$ ($0 \leq x \leq 0.22$) were grown using a Sn and Pb mixed flux (see Supplemental Material, Sec. I [16]). Figure 1(a) shows a rhombohedral structure with a space group of R-3m (No. 166) for $Co_3Sn_2S_2$. The crystal possesses quasi-two-dimensional Co_3Sn layers sandwiched between S atoms, with Ni atoms randomly replacing Co atoms on the kagome lattices. The magnetic moments are mainly located on the Co atoms of the kagome layer and align along the c axis. The saturation magnetization (M_S) and Curie temperature (T_C) decreased with an increase in the Ni content (see Fig. S2 and Table S2 in Sec. II of Supplemental Material [16]), which is mainly attributed to the weaker spin splitting and exchange interaction of Ni than that of Co. The temperature dependence of the longitudinal resistivity (ρ_{xx}) for $I//a$ and $H = 0$ shows a rapid drop below the kink point T_C, as shown in Fig. 1(b). The residual resistivity shows a minimum at $x = 0.05$ (see Supplemental Material, Sec. III [16]), which is attributed to the competition between the E_F shift and the effect of the disorder in this topological semimetal.

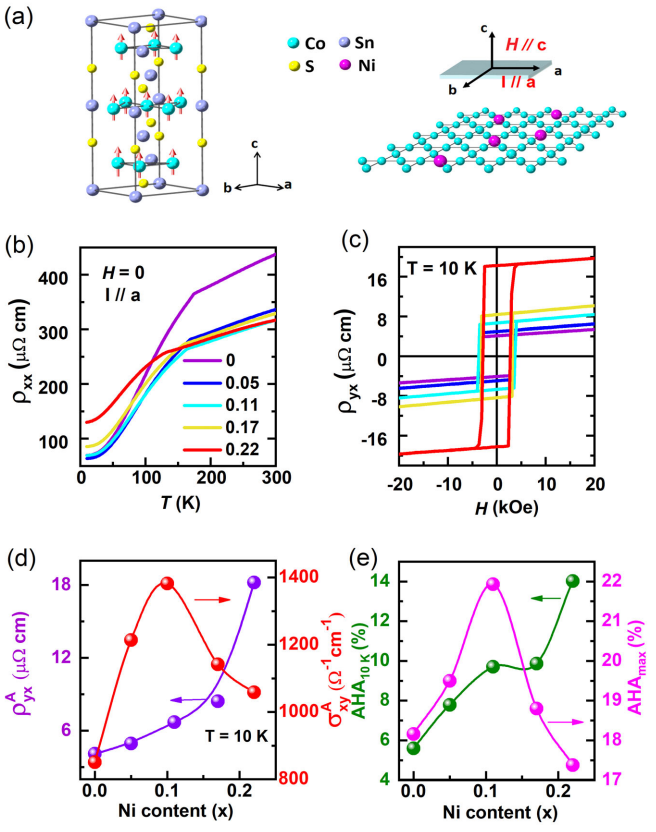

FIG. 1. (a) Crystal structure of $Co_3Sn_2S_2$ and a kagome layer composed of Co/Ni atoms. Inset above the kagome layer is the configuration for the transport measurements. (b) Temperature dependence of ρ_{xx} for different Ni contents. (c) Magnetic field dependence of ρ_{yx} for $H//c$ and $I//a$. (d) Ni content dependence of ρ^A_{yx} and σ^A_{xy}. (e) Ni content dependence of AHA at 10 K and maximal values of AHA.

Figure 1(c) shows the Hall resistivity (ρ_{yx}) as a function of the magnetic field at 10 K under the configuration of $H//c$ and $I//a$. The anomalous Hall resistivities ρ^A_{yx} are then obtained as the zero-field extrapolation of the high-field part. With an increase in the amount of Ni, ρ^A_{yx} at 10 K clearly increases from 4.0 $\mu\Omega$ cm at $x = 0$ to 18.2 $\mu\Omega$ cm at $x = 0.22$, as shown in Fig. 1(d). The anomalous Hall conductivity (σ^A_{xy}) can be further calculated using ρ_{xx} and ρ^A_{yx} through the relation $\sigma^A_{xy} = \rho^A_{yx}/[(\rho^A_{yx})^2 + \rho^2_{xx}]$. The results at 10 K show an initial increase and a subsequent decrease with an increase in the Ni content, forming a maximal value of 1382 Ω^{-1} cm^{-1} at $x = 0.11$ [Fig. 1(d)]. The prominent enhancement from 850 to 1382 Ω^{-1} cm^{-1} shows an increase of more than 60% at low doping levels. As an important measure of the Hall transport properties, the AHA reflects the conversion efficiency of the longitudinal current into the transverse current, which can be characterized by $\sigma^A_{xy}/\sigma_{xx}$. With an increase in the Ni content, the AHA increases up to 14% at 10 K, showing a small peak at $x = 0.11$, as indicated in Fig. 1(e). The temperature dependence of the AHA can be obtained from the $\rho_{yx}(H)$ data measured at different temperatures (see Supplemental Material, Sec. IV [16]). For each Ni content, the maximal value of the AHA is also shown in Fig. 1(e). Clearly, a sharp peak in the AHA appears, with a maximal value of 22% also at $x = 0.11$, which is higher than that of undoped $Co_3Sn_2S_2$. These experimental results unambiguously show that approximately 3.7% Ni doping of Co atoms in topological Weyl semimetal $Co_3Sn_2S_2$ leads to a significant enhancement of the AHC, indicating that the manipulation of the Berry curvature through chemical doping is more complicated in a rigid band model than previously thought.

In general, an AHE can result from both the intrinsic effect of the Berry curvature and extrinsic effects such as skew scattering and side jump [15]. To quantitatively reveal the contributions of the intrinsic and extrinsic mechanisms, the TYJ scaling model [47,48] was adopted, where the

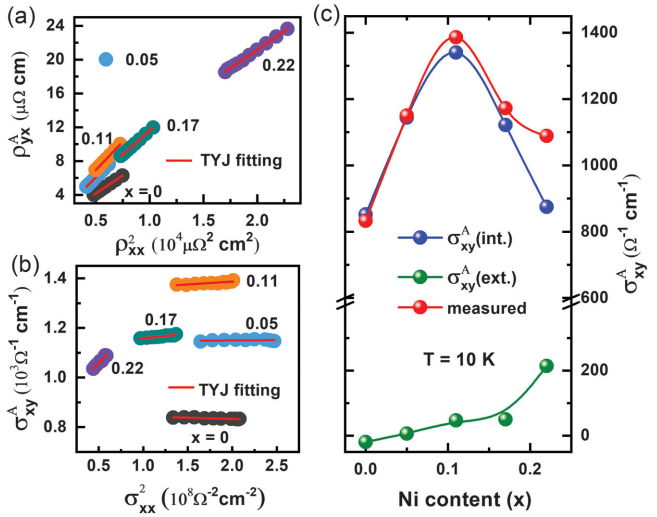

FIG. 2. Fittings of (a) ρ_{xx}^2 dependence of ρ_{yx}^A and (b) σ_{xx}^2 dependence of σ_{xy}^A using TYJ model, and (c) Ni content dependences of intrinsic and extrinsic AHCs, separated by the TYJ model from the total measured AHC at 10 K.

temperature-dependent component in the extrinsic contribution was dissociated, leaving the residual resistivity component at zero temperature as the unique extrinsic contribution. With the $\rho_{yx}^A = a\rho_{xx0} + b\rho_{xx}^2$ scaling, where ρ_{xx0} is the residual resistivity, the TYJ model has been widely used in many systems [36,49–51]. In this model, the first item on the right side of the equation comes from the contribution of the extrinsic mechanism, while the second item comes from the intrinsic contribution. From this scaling, a linear relationship can be expected between ρ_{yx}^A and ρ_{xx}^2, which is indeed seen with the best fitting in Fig. 2(a). Meanwhile, the TYJ model can also be expressed as $\sigma_{xy}^A = -a\sigma_{xx0}^{-1}\sigma_{xx}^2 - b$, where $\sigma_{xx0} = 1/\rho_{xx0}$ and b are the residual conductivity and intrinsic σ_{xy}^A, respectively. Figure 2(b) also shows the linear relationship between σ_{xy}^A and σ_{xx}^2 for different Ni contents, with the intrinsic σ_{xy}^A values obtained by intercept b on the longitudinal axis. As shown in Fig. 2(c), intrinsic $\sigma_{xy}^A[\sigma_{xy}^A(\text{int.})]$ first increases and then decreases with an increase in the Ni content, also forming a maximum of 1340 $\Omega^{-1}\,\text{cm}^{-1}$ at $x = 0.11$, whereas further increasing the Ni content leads to a decrease in $\sigma_{xy}^A(\text{int.})$. The peaks of $\sigma_{xy}^A(\text{int.})$ and the measured total σ_{xy}^A overlap each other within the doping range of $x = 0$–0.17. Meanwhile, during the Ni doping, the extrinsic $\sigma_{xy}^A[\sigma_{xy}^A(\text{ext.})]$ basically remains at approximately zero and increases slowly to 214 $\Omega^{-1}\,\text{cm}^{-1}$ at $x = 0.22$. Therefore, the TYJ model indicates that the AHC of $Co_{3-x}Ni_xSn_2S_2$ is mainly enhanced by the intrinsic contribution from electronic structures, and the extrinsic contribution by impurity scattering of Ni dopants is very weak. A careful examination of the fittings in Fig. 2(b) shows small deviations at low temperatures for the doped compositions, which indicates that a slight extrinsic contribution of the side-jump mechanism may also be introduced through doping [48].

Having established that the observed AHC enhancement is caused by a tailoring of the Berry curvature, we next applied an atomistic description of chemical doping using a state-of-the-art density functional theory approach to gain a fundamental picture of such a doping-induced AHC modulation. In general, electron doping means that E_F shifts toward the conduction band. However, such a definition naturally assumes a rigid band model that is inactive to the doping process. By contrast, pushing E_F to higher energy levels often leads to reactions of an electronic structure, such as polarons, demonstrating a coupling between the carriers and lattice distortions [52,53]. Moreover, the global electronic structure of a chemical-doped sample should be the average of many locally distorted configurations, rather than the property of an averaged, distortion-free configuration [54–56]. Therefore, a comprehensive description of the doping, particularly for quantities such as Berry curvature, which is sensitive to the electronic structure, should consider multiple local configurations. Thus, we constructed large supercells to capture the experimental conditions after doping, including disorder effects, local environments, and translational-symmetry breaking (see Supplemental Material, Sec. V [16]). We then used the "effective band structure" (EBS) method [57–60] to unfold the sophisticated $E - k$ dispersion within a small supercell BZ into the spectrum density in the primitive BZ.

The band structure of pristine $Co_3Sn_2S_2$ is shown in Fig. 3(a). With SOC, the nodal lines of the $Co_3Sn_2S_2$ caused by band inversion are all gapped except for Weyl points, which is in agreement with previous studies [4,5]. In slightly Ni-doped $Co_3Sn_2S_2$ ($x = 0.056$), extra electron filling moves E_F up macroscopically, as expected in Fig. 3(b). Remarkably, owing to a local distortion, a special form of disorder effect is induced through doping. Figure 3(b) also shows significant band splitting along both the U–L and $L - \Gamma$ paths. Such splitting can broaden the band spectra and thus reduce the inverted gap. More dopants further shift E_F upwards and enhance the band broadening, as shown in Fig. 3(c) (also see Supplemental Material, Sec. VI [16]). Recall that the AHC depends on both the inverted gap and the position of E_F, and the synergic effect of the E_F movement and gap narrowing determines the evolution of AHC upon doping.

As shown in Fig. 3(d), the calculated peak value of the energy-dependent AHC of pristine $Co_3Sn_2S_2$ is located exactly at E_F. If we resort to the rigid band model [10], the Co substitution from Ni introduces extra electrons and thus moves E_F to higher energies, and the AHC should decreases accordingly, as mentioned earlier. We then applied the virtual crystal approximation (VCA) approach [27,28], which considers a symmetry-preserved primitive cell composed of "virtual" atoms (see Supplemental Material, Sec. V [16]). Compared with the rigid band

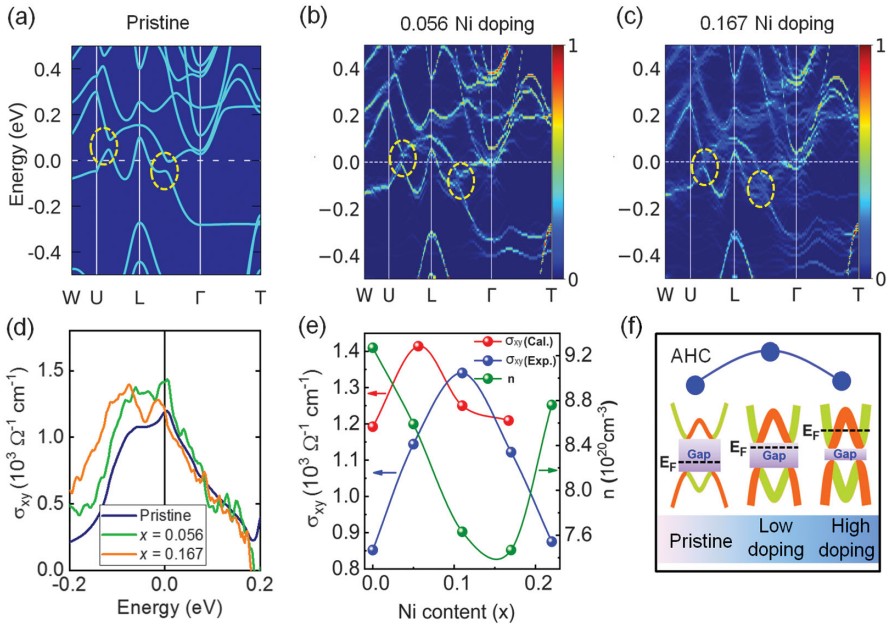

FIG. 3. (a) Band structures of pristine $Co_3Sn_2S_2$. (b),(c) Effective band structures for $x = 0.056$ and 0.167 Ni-doped $Co_3Sn_2S_2$, respectively. Dashed yellow ellipses in (a)–(c) highlight the band splitting along the U–L and $L-\Gamma$ paths. The color scale in (b),(c) represents the spectral weight of the $\boldsymbol{k}$ character for the primitive Brillouin zone. (d) Energy-dependent AHC of pristine, $x = 0.056$ and 0.167 Ni-doped $Co_3Sn_2S_2$. (e) Evolution of the AHC as a function of doping content from the calculations and experiments (left), and carrier density (n) dependence of Ni content (right). (f) Schematic plot showing the modulation effects of the band structure and the resultant AHC upon Ni doping. SOC was included for all calculations.

model, VCA yields slight band dynamics (mainly around the L point, see Supplemental Material, Sec. VII [16]) upon doping. However, it excludes the doping-induced local disorder effects. As a result, the main factor affecting the calculated AHC is the E_F movement, leading to a slight enhancement at $x = 0.056$ and then decreases monotonically with a further increase in the Ni doping (see Supplemental Material, Sec. VII [16]). In comparison, our supercell approach predicted a more profound AHC elevation at $x = 0.056$, indicating that the doping-induced modulation of the electronic structure is indeed important to enhance the Berry curvature. The corresponding maximum evolution of AHC is comparable with that of the intrinsic component decomposed from the measured AHC, as shown in Fig. 3(e). A possible reason for the slight shift in the peak positions may originate from more complicated defects in the real materials. Meanwhile, the carrier density, extracted by fitting the ordinary Hall part from Fig. 1(c), shows a clear minimum at around $x = 0.15$ [Fig. 3(e)], which indicates that doping Ni moves the E_F into the inverted gap. Thus, the enhancement of the intrinsic AHC is accompanied by a decrease in the carrier density. It can be further seen that the peak of the AHC is located within the valence band just below the gap, which provides a subtle relation between the inverted gap and Berry-phase dominated AHC in the present system.

Overall, our supercell approach captures both the E_F-shifting effect from extra electron filling and the band broadening effect from local disorder. The former (latter) factor tends to reduce (enhance) the intrinsic contribution to the AHC of $Co_3Sn_2S_2$, leading to a competing mechanism of the evolution of the intrinsic AHC, as illustrated in Fig. 3(f). At low doping levels, the total AHC is dominated by the gap narrowing from the band broadening, leading to an increasing trend. Consequently, this effect will be remarkable in topological materials when E_F lies within the inverted gap. However, at high doping levels, E_F moves away from the inverted gap region and thus strongly suppresses the total AHC despite an even smaller inverted gap. Similar supercell approaches were applied to Fe-Co alloys, where the E_F-shifting and band smearing effects are responsible for the AHC reduction at a 25% Co composition [61].

From a conventional viewpoint [15], the AHE is proportional to M according to $\rho_{yx} = \rho^N_{yx} + \rho^A_{yx} = R_0 H + 4\pi R_S M$, where R_0, H, R_S, and M denote the ordinary Hall coefficient, magnetic field, anomalous Hall coefficient, and magnetization, respectively. However, as the first experimentally confirmed magnetic Weyl semimetal, $Co_3Sn_2S_2$ exhibits a significant AHE [4] and an anomalous Nernst effect [62] owing to the nontrivial Berry curvature. As a result, the significant AHC and AHA in pristine $Co_3Sn_2S_2$ are accompanied by a small M of only 0.92 μ_B/f.u., which is lower than that of many ferromagnetic materials. The anomalous Hall factor (S_H), defined by σ^A_{xy} per unit of magnetic moment (σ^A_{xy}/M), is as high as 1.1 V^{-1} (Fig. 4), which is 1–2 orders

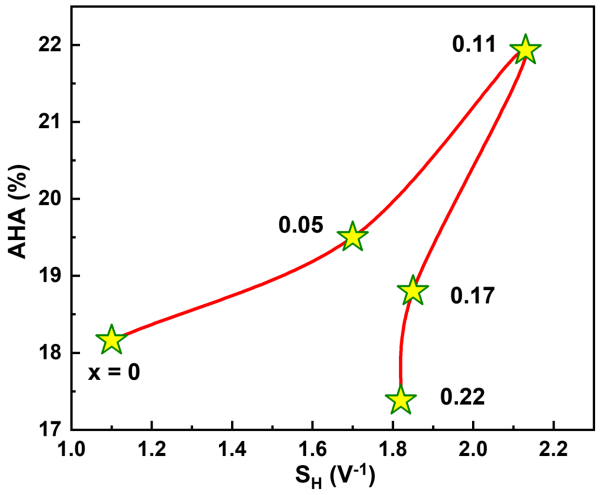

FIG. 4. Maximal AHA and S_H of $Co_{3-x}Ni_xSn_2S_2$. Enhancements in AHA and S_H were obtained through a local disorder from Ni doping.

in magnitude higher than that of many AHE materials. With the disorder-enhanced Berry curvature upon Ni doping, the AHA was further enhanced to 22% at $x = 0.11$ (Fig. 4). Meanwhile, S_H is also improved to a maximal value of 2.3 V^{-1} at $x = 0.11$ (Fig. 4), which is twice as large as that of pristine $Co_3Sn_2S_2$. Such a large enhancement of S_H is attributed to both the increased AHC and the reduced M owing to the lower magnetic moments of Ni than those of Co atoms (see Supplemental Material, Secs. II and VIII [16]). Both the S_H and AHA values in Ni-doped $Co_3Sn_2S_2$ are much larger than those of many AHE materials (see Supplemental Material, Sec. IX [16]).

In summary, in Ni-doped magnetic Weyl semimetal $Co_3Sn_2S_2$, elevations of AHC (~1400 Ω^{-1} cm^{-1}), AHA (~22%), and S_H (~2.3 V^{-1}) were achieved through the doping-induced modulation of the topological band structures. The separation of intrinsic and extrinsic contributions based on the TYJ model indicates that the enhancement of AHE is mainly attributed to the intrinsic mechanism. Theoretical calculations reveal that the increase in the intrinsic contribution, dictated by the Berry curvature, originates from the broadening of the inverted bands caused by the local disorder effect. Such a mechanism, together with the extra electron filling shifting E_F, leads to a collaborative modulation of the AHE observed in Ni-doped $Co_3Sn_2S_2$. Our findings provide a novel understanding of the local disorder effect of chemical doping on the modulation of topological bands, which also sheds light on the relevant electronic, thermal, or optical properties in emerging topological materials.

This work was supported by National Key R&D Program of China (2019YFA0704900 and 2017YFA0206300), National Natural Science Foundation of China (11974394), the Strategic Priority Research Program (B) of the Chinese Academy of Sciences (CAS) (XDB33000000), Beijing Natural Science Foundation (Z190009), Users with Excellence Program of Hefei Science Center CAS (2019HSC-UE009), Youth Innovation Promotion Association of CAS (2013002), Fujian Institute of Innovation CAS, Guangdong Innovative and Entrepreneurial Research Team Program (2017ZT07C062), the Guangdong Provincial Key Laboratory of Computational Science and Material Design (2019B030301001), the Science, Technology and Innovation Commission of Shenzhen Municipality (ZDSYS20190902092905285) and Center for Computational Science and Engineering of Southern University of Science and Technology.

*These authors contributed equally to this work.
†liuqh@sustech.edu.cn
‡ekliu@iphy.ac.cn

[1] Z. Fang *et al.*, Science **302**, 92 (2003).
[2] D. Xiao, M. C. Chang, and Q. Niu, Rev. Mod. Phys. **82**, 1959 (2010).
[3] G. Sundaram and Q. Niu, Phys. Rev. B **59**, 14915 (1999).
[4] E. K. Liu *et al.*, Nat. Phys. **14**, 1125 (2018).
[5] Q. Wang, Y. Xu, R. Lou, Z. Liu, M. Li, Y. Huang, D. Shen, H. Weng, S. Wang, and H. Lei, Nat. Commun. **9**, 3681 (2018).
[6] D. F. Liu *et al.*, Science **365**, 1282 (2019).
[7] N. Morali, R. Batabyal, P. K. Nag, E. Liu, Q. Xu, Y. Sun, B. Yan, C. Felser, N. Avraham, and H. Beidenkopf, Science **365**, 1286 (2019).
[8] H. M. Weng, Sci. China-Phys. Mech. Astron. **62**, 127031 (2019).
[9] D. J. Thouless, M. Kohmoto, M. P. Nightingale, and M. den Nijs, Phys. Rev. Lett. **49**, 405 (1982).
[10] E. A. Stern, Phys. Rev. **157**, 544 (1967).
[11] S. Thiel, G. Hammerl, A. Schmehl, C. W. Schneider, and J. Mannhart, Science **313**, 1942 (2006).
[12] A. M. Ionescu and H. Riel, Nature (London) **479**, 329 (2011).
[13] S. Kastbjerg, N. Bindzus, M. Søndergaard, S. Johnsen, N. Lock, M. Christensen, M. Takata, M. A. Spackman, and B. B. Iversen, Adv. Funct. Mater. **23**, 5477 (2013).
[14] Z. Wang, Q. Liu, J.-W. Luo, and A. Zunger, Mater. Horiz. **6**, 2124 (2019).
[15] N. Nagaosa, J. Sinova, S. Onoda, A. H. MacDonald, and N. P. Ong, Rev. Mod. Phys. **82**, 1539 (2010).
[16] See Supplemental Material at http://link.aps.org/supplemental/10.1103/PhysRevLett.125.086602 for details of determination of single crystal composition, magnetic measurements, residual resistivity, carrier density, mobility of $Co_{3-x}Ni_xSn_2S_2$, and details of temperature dependence of Hall resistivity, and details of the first-principles calculations, which includes Refs. [2, 17–35], EBS and AHC of Ni doped $Co_3Sn_2S_2$ with supercell approach, band structures and AHCs of doped $Co_3Sn_2S_2$ with VCA approach, calculated magnetic moments of Ni and Co atoms with supercell approach, and details of comparison of the anomalous Hall angles and anomalous Hall factors between $Co_{3-x}Ni_xSn_2S_2$ and

other anomalous Hall effect materials, which includes Refs. [1,36–46].
[17] P. Hohenberg and W. Kohn, Phys. Rev. **136**, B864 (1964).
[18] W. Kohn and L. J. Sham, Phys. Rev. **140**, A1133 (1965).
[19] J. P. Perdew, K. Burke, and M. Ernzerhof, Phys. Rev. Lett. **77**, 3865 (1996).
[20] J. P. Perdew, K. Burke, and M. Ernzerhof, Phys. Rev. Lett. **78**, 1396 (1997).
[21] G. Kresse and J. Furthmüller, Phys. Rev. B **54**, 11169 (1996).
[22] G. Kresse and D. Joubert, Phys. Rev. B **59**, 1758 (1999).
[23] P. V. C. Medeiros, S. Stafström, and J. Björk, Phys. Rev. B **89**, 041407(R) (2014).
[24] P. V. C. Medeiros, S. S. Tsirkin, S. Stafström, and J. Björk, Phys. Rev. B **91**, 041116(R) (2015).
[25] K. Momma and F. Izumi, J. Appl. Crystallogr. **44**, 1272 (2011).
[26] V. Wang, N. Xu, J. Liu, G. Tang, and W. Geng, arXiv:1908.08269.
[27] L. Nordheim, Ann. Phys. (N.Y.) **401**, 607 (1931).
[28] L. Bellaiche and D. Vanderbilt, Phys. Rev. B **61**, 7877 (2000).
[29] P. Giannozzi *et al.*, J. Phys. Condens. Matter **21**, 395502 (2009).
[30] P. Giannozzi *et al.*, J. Phys. Condens. Matter **29**, 465901 (2017).
[31] A. Dal Corso, Comput. Mater. Sci. **95**, 337 (2014).
[32] N. Marzari and D. Vanderbilt, Phys. Rev. B **56**, 12847 (1997).
[33] I. Souza, N. Marzari, and D. Vanderbilt, Phys. Rev. B **65**, 035109 (2001).
[34] A. A. Mostofi, J. R. Yates, G. Pizzi, Y.-S. Lee, I. Souza, D. Vanderbilt, and N. Marzari, Comput. Phys. Commun. **185**, 2309 (2014).
[35] Q. Wu, S. Zhang, H.-F. Song, M. Troyer, and A. A. Soluyanov, Comput. Phys. Commun. **224**, 405 (2018).
[36] I. Belopolski *et al.*, Science **365**, 1278 (2019).
[37] S. Iguchi, N. Hanasaki, and Y. Tokura, Phys. Rev. Lett. **99**, 077202 (2007).
[38] F. Matsukura, H. Ohno, A. Shen, and Y. Sugawara, Phys. Rev. B **57**, R2037 (1998).
[39] K. Kim *et al.*, Nat. Mater. **17**, 794 (2018).
[40] S. Nakatsuji, N. Kiyohara, and T. Higo, Nature (London) **527**, 212 (2015).
[41] Q. Wang, S. Sun, X. Zhang, F. Pang, and H. Lei, Phys. Rev. B **94**, 075135 (2016).
[42] J. G. Checkelsky, M. Lee, E. Morosan, R. J. Cava, and N. P. Ong, Phys. Rev. B **77**, 014433 (2008).
[43] P. Matl, N. P. Ong, Y. F. Yan, Y. Q. Li, D. Studebaker, T. Baum, and G. Doubinina, Phys. Rev. B **57**, 10248 (1998).
[44] M. Lee, Y. Onose, Y. Tokura, and N. P. Ong, Phys. Rev. B **75**, 172403 (2007).
[45] A. Sakai *et al.*, Nat. Phys. **14**, 1119 (2018).
[46] C. Sürgers, G. Fischer, P. Winkel, and H. v. Löhneysen, Phys. Rev. B **90**, 104421 (2014).
[47] Y. Tian, L. Ye, and X. Jin, Phys. Rev. Lett. **103**, 087206 (2009).
[48] D. Hou, G. Su, Y. Tian, X. Jin, S. A. Yang, and Q. Niu, Phys. Rev. Lett. **114**, 217203 (2015).
[49] L. Ye, Y. Tian, X. Jin, and D. Xiao, Phys. Rev. B **85**, 220403 (R) (2012).
[50] P. He, L. Ma, Z. Shi, G. Y. Guo, J.-G. Zheng, Y. Xin, and S. M. Zhou, Phys. Rev. Lett. **109**, 066402 (2012).
[51] L. Ye *et al.*, Nature (London) **555**, 638 (2018).
[52] Q. H. Liu, Q. Yao, Z. A. Kelly, C. M. Pasco, T. M. McQueen, S. Lany, and A. Zunger, Phys. Rev. Lett. **121**, 186402 (2018).
[53] X. Zhang, L. B. Abdalla, Q. Liu, and A. Zunger, Adv. Funct. Mater. **27**, 1701266 (2017).
[54] A. Zunger, S. H. Wei, L. G. Ferreira, and J. E. Bernard, Phys. Rev. Lett. **65**, 353 (1990).
[55] S. H. Wei, L. G. Ferreira, J. E. Bernard, and A. Zunger, Phys. Rev. B **42**, 9622 (1990).
[56] L. W. Wang, L. Bellaiche, S. H. Wei, and A. Zunger, Phys. Rev. Lett. **80**, 4725 (1998).
[57] T. B. Boykin and G. Klimeck, Phys. Rev. B **71**, 115215 (2005).
[58] T. B. Boykin, N. Kharche, G. Klimeck, and M. Korkusinski, J. Phys. Condens. Matter **19**, 036203 (2007).
[59] V. Popescu and A. Zunger, Phys. Rev. Lett. **104**, 236403 (2010).
[60] V. Popescu and A. Zunger, Phys. Rev. B **85**, 085201 (2012).
[61] R. Bianco, R. Resta, and I. Souza, Phys. Rev. B **90**, 125153 (2014).
[62] S. N. Guin *et al.*, Adv. Mater. **31**, 1806622 (2019).